

## Table of contents

### Experimental sections

1. Material preparation
2. Characterizations
3. Transformation and Crystallization Kinetics
4. Morphological transformation of MOF gel

### Supplementary Figures

- Fig. S1. Molecular diffusion through metal precursor gel.  
Fig. S2. Mechanical strengths of MOF aerogels.  
Fig. S3. Transformation of ZIF-8 from Zn precursor gel characterized by ex-situ XRD.  
Fig. S4. Sharp-Hancock plots for the ZIF-8 crystallization from Zn precursor gel at different temperatures.  
Fig. S5. Gel network dissolution during ZIF-8 transformation.  
Fig. S6. Gel transformation from Zn, Ni, Al, Fe, and Co-MOF metal precursor gels to their MOFs.  
Fig. S7. SEM images of MOF aerogels and their characteristic crystal shapes.  
Fig. S8. Morphological transformation of Cu precursor gel to HKUST-1 at different conditions vs time.  
Fig. S9. HKUST-1 crystallization at different conditions  
Fig. S10. HKUST-1 crystal growth in gel networks.  
Fig. S11. Dissolution of Cu precursor gel network during transformation into HKUST-1 in different conditions.  
Fig. S12. Rheological properties of metal gels of Zn, Ni, Cu, Co, Fe, Eu, and Al with addition of different amount of PAA (0-12wt.%).  
Fig. S13. Sol-gel 3D-printer.  
Fig. S14. Dynamic strain sweeps of metal gels and their converted MOF gels.

### Supplementary Tables

- Table S1. Preparation of Zn precursor gels.  
Table S2. FTIR band assignments for Zn precursor aerogel, ZIF-8 and MOF-5 aerogels.  
Table S3. Textural properties of freestanding porous MOFs, silica, and carbon materials.  
Table S4. ZIF-8 crystallization rate kinetics according to Avrami–Erofe’ev equation.  
Table S5. ZIF-8 crystallization rate kinetics according to Gualtieri equation.  
Table S6. Zinc dissolution from precursor gels according to a first order rate law.  
Table S7. Preparation of aluminum, nickel, iron, cobalt, copper, and europium precursor gels.  
Table S8. Preparation of MOF gels/aerogels from their respective metal precursor gels.  
Table S9. HKUST-1 crystallization rate kinetics according to Gualtieri equation.  
Table S10. Copper dissolution from precursor alcogels according to a first order rate law.

## Experimental sections

### 1. Material preparation

#### Metal precursor gels

The metal salt(s) (0.6 mmol) were dissolved in 1 ml solvent containing polyacrylic acid (0-8.0 wt.%), and 4-8 mmol propylene oxide was added (Table S1). The resulting solution was vigorously mixed and allowed to react and form a gel.

#### MOF gels

The organic ligand was dissolved in an appropriate solvent. A gradual solvent exchange process replaced the alcohol in the metal precursor gel with the solvent for 24-36 h at room temperature. The metal precursor gel was then immersed in the organic ligand solution at the conversion temperature for 36-72 h (Table S8).

#### MOF aerogels

The MOF solvogel underwent gradual solvent-exchange to acetone prior to CO<sub>2</sub> supercritical extraction and drying. Acetone is extracted by liquid CO<sub>2</sub> at 298 K and 5.8 MPa. The vessel was heated slowly to 323 K with a concomitant increase in pressure to 9 MPa. The vessel was kept at this condition for 24 h before releasing the CO<sub>2</sub> at a rate of 2 MPa/h. After cooling the vessel to room temperature, the MOF aerogel was weighed and stored in a clean container.

#### 3D printing sol-gel metal precursor

A laboratory-designed and -built 3D printer shown in Fig. S13 uses the frame of a commercial 3D printer (mGiraffe DIY 3D Delta Printer) with a reprogrammed controller (Marlin Mega 2560) for precision printing. An advanced extruder applies a maximum torque of 71 N.cm to extrude 12.5 nL volume of sol-gel for each step of the motor. The extruder's xyz position is controlled by Nema 17 motors and together with 18T pulley teeth and 2 mm belt pitch gives a 5.6 μm spatial resolution. The mechanical framework can accommodate a printing volume of D90 x 150 mm with a top printing speed of 0.8 mm<sup>3</sup>/s. The printing speed for metal sol-gel was 3 mm.s<sup>-1</sup> using a 0.6 mm extruder nozzle at a height of 0.6 mm from the printing surface to deposit 650 μm thick patterned layer. Zn, Cu, Al, Ni, Fe, Eu, and Co sol-gels were printed into a two-layered or multi-layered 3D 90-degree grid structures and were respectively transformed into MOFs by immersing in appropriate ligand solutions.

#### Examples: ZIF-8 and MOF-5 aerogels

##### Zn precursor gel

0.65 mmol Zn(NO<sub>3</sub>)<sub>2</sub>·6H<sub>2</sub>O and 0.15 mmol ZnCl<sub>2</sub> were dissolved in ethanol along with 0.0178 mmol PAA to produce a 1.3 ml clear solution to which 8 mmol propylene oxide was added. The mixture was vigorously shaken for a minute and allowed to react and form a solid gel in 24 min.

##### ZIF-8 aerogel

2-methylimidazole (Hmim) was dissolved in methanol to give a 0.3 M solution. The Zn precursor alcogel was solvent exchanged thrice with methanol over 24 h, before immersing in 15 ml 0.3 M Hmim in methanol solution. The conversion proceeded at room temperature for 36 h. This was followed by solvent exchange with methanol thrice, followed thrice with 3:1, 1:1, and 1:3 methanol-acetone solutions, respectively. A final solvent exchange with pure acetone was conducted before CO<sub>2</sub> supercritical drying. It is important to note that Hmim was also prepared in dimethyl formamide (DMF), ethanol, and water for preparing the corresponding ZIF-8 solvogel.

##### MOF-5 aerogel

A 0.075 M terephthalic acid (H<sub>2</sub>BDC) in DMF was prepared with care given that water and alkali can interfere with MOF-5 crystallization. The Zn precursor alcogel was exchanged thrice with DMF over 24 h before immersing in 20 ml 0.075 M H<sub>2</sub>BDC. The pH was adjusted to 5.4 by adding drops of 1 M HCl. The conversion proceeded at room temperature for 48 h. This was followed by solvent exchange with DMF thrice, followed thrice with 3:1, 1:1, and 1:3 DMF-acetone solutions, respectively. A final solvent exchange with pure acetone was conducted before CO<sub>2</sub> supercritical drying.

### **Examples: 3D printed HKUST-1 90° grid scaffold**

#### **Cu precursor gel**

1.5 mmol  $\text{CuCl}_2 \cdot 2\text{H}_2\text{O}$  was dissolved in 1 ml ethanol along with 0.02 mmol PAA to produce a 1.1 ml solution to which 5 mmol propylene oxide was added. The mixture was vigorously shaken for a minute and allowed to react and form a solid gel in 15 min. The viscosity can be adjusted by varying addition amount of PAA.

#### **3D printing Cu precursor gel into multi-length scale complex architecture**

The 3D printing of the gel was conducted using the 3D printing system in Fig. S13 and described above. In detail, ca.  $3 \text{ cm}^3$  of the gel was loaded into a 5ml syringe with a nozzle of 20G (ID: 600  $\mu\text{m}$ ) at an extrusion rate of  $0.8 \text{ mm}^3 \cdot \text{s}^{-1}$  and printing speed of  $3 \text{ mm} \cdot \text{s}^{-1}$  at a height of 0.6 mm from the printing surface to deposit 650  $\mu\text{m}$  thick patterned layer. A 3D 90° grid scaffold of multilength scale with dimension of  $17\text{mm} \times 17\text{mm} \times 8\text{mm}$  was obtained within 12min.

#### **Transformation of the printed Cu gel into HKUST-1 complex architecture**

Trimesic acid (TMA) was dissolved in ethanol/ $\text{H}_2\text{O}$  (1:1) to give a 0.35 M solution. The 3D printed Cu gel scaffold was solvent exchanged thrice with ethanol, ethanol/ $\text{H}_2\text{O}$  (2:1), and ethanol/ $\text{H}_2\text{O}$  (1:1) within 24 h, before immersing in 20 ml 0.35 M TMA solution. The conversion proceeded at room temperature for 36 h. This was followed by solvent exchange with ethanol/ $\text{H}_2\text{O}$  (1:1) thrice to remove unreacted ligands. A final solvent exchange with pure acetone was conducted before  $\text{CO}_2$  supercritical drying for obtaining aerogel sample, while a direct ambient drying was performed following thrice washing with ethanol for obtaining porous monolith sample with 1/2 shrinkage in length but improved mechanical strength.

## **2. Characterizations**

The structure, morphology, and textural properties of the metal precursor and MOF aerogels were analyzed by PANalytical X'pert Pro powder X-ray diffractometer, JEOL 7100F scanning electron microscope, and Beckman Coulter SA3100 surface area and pore size analyzer. The X-ray diffraction of powder samples was collected for  $2\theta$  of 4 to  $45^\circ$  using monochromatic  $\text{Cu K}\alpha 1$  radiation in transmission geometry, at a step of  $0.0833^\circ$ , with an accumulation time of 480 s per step. Samples were mounted on a copper sample holder with conducting copper tape and sputter-coated with a thin layer of gold for observation under SEM at an accelerating voltage of 8-10 kV. The  $\text{N}_2$  adsorption/desorption isotherms were measured at 77 K after sample outgassing at  $120^\circ\text{C}$  for 150 min. The Langmuir and BET surface area, total pore volume, and pore size distribution were determined from the isotherms. The samples were also observed under JEOL JEM 2010F transmission electron microscope at an accelerating voltage of 120 kV. Information on gel network and pore structure were obtained by Cryogenic Dual Beam Nova 200 FIB/SEM equipped with a 30 kV field emission gun column and a Ga-based 30 kV ion column.

The material chemistry and composition were determined by Renishaw InVia Micro-Raman/Photoluminescence System and Bruker Vertex 70 Hyperion 1000 FTIR. The Raman spectra were collected from powder samples deposited on clean glass from 400 to  $4000 \text{ cm}^{-1}$  with a 50 mW Ar ion laser (514.5 nm). The FTIR-ATR spectra were recorded from powder samples from 400 to  $4000 \text{ cm}^{-1}$ . The thermal, mechanical, and transport properties of the samples were also measured. Thermogravimetric analysis (TGA) was conducted in Perkin Elmer DTA 7 with the samples heated from room temperature to  $800^\circ\text{C}$  at a heating rate of  $10^\circ\text{C min}^{-1}$  in air. Thermal conductivity was determined by placing the sample on a heated aluminum block kept at  $300^\circ\text{C}$ , and the temperature of the sample was monitored with a pair of K-type thermocouples and by NEC Thermo Tracer TH7800N thermal camera. The mechanical properties were measured by Instron 5567 universal tester, while oxygen (UHP, Linde HKO) permeation and diffusion were measured in a gas permeation and home-made Wicke-Kallenbach diffusion cell.

### 3. Transformation and Crystallization Kinetics

Thin 30  $\mu\text{m}$  thick metal precursor gels were crystallized by immersing in solutions of organic ligands at a given temperature and prescribed length of time before quenching in an excess fresh solvent. Perkin Elmer Lambda 20 UV-Vis spectrophotometer confirmed complete ligand removal before X-ray diffraction. The extent of crystallization  $\alpha(t)$  was determined from the ratio of normalized intensity ( $I$ ) of the characteristic diffraction peak to its maximum intensity ( $I_{max}$ ) at the end of the conversion. The crystallization curves were obtained by the Sharp and Hancock (SH) method<sup>1</sup> based on the linearization of Avrami–Erofe'ev (AE) equation as shown in Eqn. 1.<sup>2,3</sup>

$$\alpha = 1 - \exp\{-[k(t - t_0)]^n\} \quad \text{Eqn. 1}$$

where  $t_0$  is the induction time,  $n$  and  $k$  are the Avrami's exponent and rate constant, respectively.

The above AE equation is linearized to obtain the Avrami's exponent ( $n$ ) and the overall rate constant ( $k$ ) in Eqn. 2.

$$\ln[-\ln(1 - \alpha)] = n \ln(k) + n \ln(t - t_0) \quad \text{Eqn. 2}$$

The MOF crystallization in this study displays  $n$  values of 0.4–0.7, indicating the diffusion-controlled process with a shrinking geometry. This is consistent with the crystallization of MOF in the gel material. The crystallization was also analyzed by the Gualtieri model<sup>4</sup> that considers a two-step crystallization process consisting of nucleation and growth as shown in Eqn. 3.

$$\alpha = \frac{1}{1 + \exp[-\frac{t-a}{b}]} \{1 - \exp[-(k_g t)^i]\} \quad \text{Eqn. 3}$$

where  $k_g$  and  $i$  are the rate constant of crystal growth and growth dimension.  $i$  is given a value of 2 for a 2D growth where the growth occurs along the contracting interface within the gel network. The  $a$  and  $b$  are constants relevant to nucleation, and can be expressed by a probability function in Eqn. 4.

$$P_N = \exp\left\{-\frac{(t-a)^2}{2b^2}\right\} \quad \text{Eqn. 4}$$

where  $a$  and  $b$  are the  $P_N$  function peak position and the variance of Gaussian distribution, respectively. The rate constant of nucleation is then given by Eqn. 5.

$$k_n = 1/a \quad \text{Eqn. 5}$$

The value of  $b$  provides insight on the nature of the nucleation process. The  $b \leq 15$  is attributed to a heterogeneous nucleation,  $b > 15$  is an autocatalytic nucleation, and  $b \sim 20$  is homogeneous nucleation.<sup>3</sup>

The ligand diffusion in precursor gel was approximated using toluene and sudan red dye of comparable molecular weight and size to Hmim and H<sub>2</sub>BDC, respectively. Measurement were made in a diffusion cell shown in Fig. S1. A 8.4 mm thick precursor gel was placed in the diffusion cell with one arm of the cell filled with pure ethanol and the other arm filled with either 0.3 M toluene in methanol or 0.3 M sudan red dye in methanol. Toluene and sudan red dye diffusing to the methanol cell were monitored by Agilent Gas Chromatograph System (7890B) and Perkin Elmer UV/VIS Spectrophotometer (Lambda 20), respectively.

The dissolution of gel network was measured during conversion by monitoring the concentration of metal precursor ions in the solution by Perkin Elmer Avio 200 Inductively Coupled Plasma-Optical Emission Spectrometer with detection limit of less than 1 ppm. The dissolution rate was fitted to a first order rate law in Eqn. 6.<sup>5,6</sup>

$$\frac{m_t}{m_\infty} = m_s \times (1 - e^{-k_d^* t}) \quad \text{Eqn. 6}$$

where  $m_t$  is the dissolved mass at time  $t$ ,  $m_\infty$  is the total mass of solid,  $m_s$  is the dissolved mass at steady state, and  $k_d^*$  is the apparent dissolution rate. The exact determination of  $k_d$  is difficult as the organic ligands can react and bind to the dissolved metal ions.

#### 4. Morphological transformation of MOF gel

HKUST-1 gel conversion is a good example as the reaction proceeds within 30min (Fig. S9). However, the morphology of HKUST-1 crystal could be changed by varying experimental conditions, which affect the gel network connectivity.

First of all, Cu precursor gel was prepared by a propylene oxide addition method similar with other metal gels mentioned in this work. Basically 1.5 mmol  $\text{CuCl}_2 \cdot 2\text{H}_2\text{O}$  was dissolved in 1.25 ml ethanol containing 4wt% PAA, subsequently 5mmol propylene oxide was added with vigorous shaking by a vortex for 2-3 seconds, gelation occurred at 2'35" to 2'42"(min./sec.).

To obtain thin film Cu precursor gels with same property for ex-situ conversion study, a dip-coating method has been employed. Surface cleaned silica wafers (6mm×6mm) were immersed in Cu precursor sols at 2'00" (after propylene oxide addition) for 15" and pulled out with a dip-coating speed of 0.5mm/s. The coated silica wafers were placed on the surface of Cu precursor gels (providing necessary volatile pressure) and sealed to allow the gels aging for 12 hours. The gels were then transferred into ligand solutions at three independent conditions of (a) [TMA] = 0.05 M, (b) [TMA] = 0.05 M, [sodium formate] = 0.10 M, and (c) [TMA] = 0.35 M, for different times upto 30min. The reaction was quenched by gently flushing the ligand solutions with excess fresh ethanol/water (1:1) for three times within 1min to largely reduce the TMA concentration on the surface of the gel, and another three times within 10min to remove residual trace amount of TMA molecules within the gel. The gels were exchanged with acetone before  $\text{CO}_2$  supercritical drying and SEM observation to study the morphological changes of HKUST-1 during transformation.

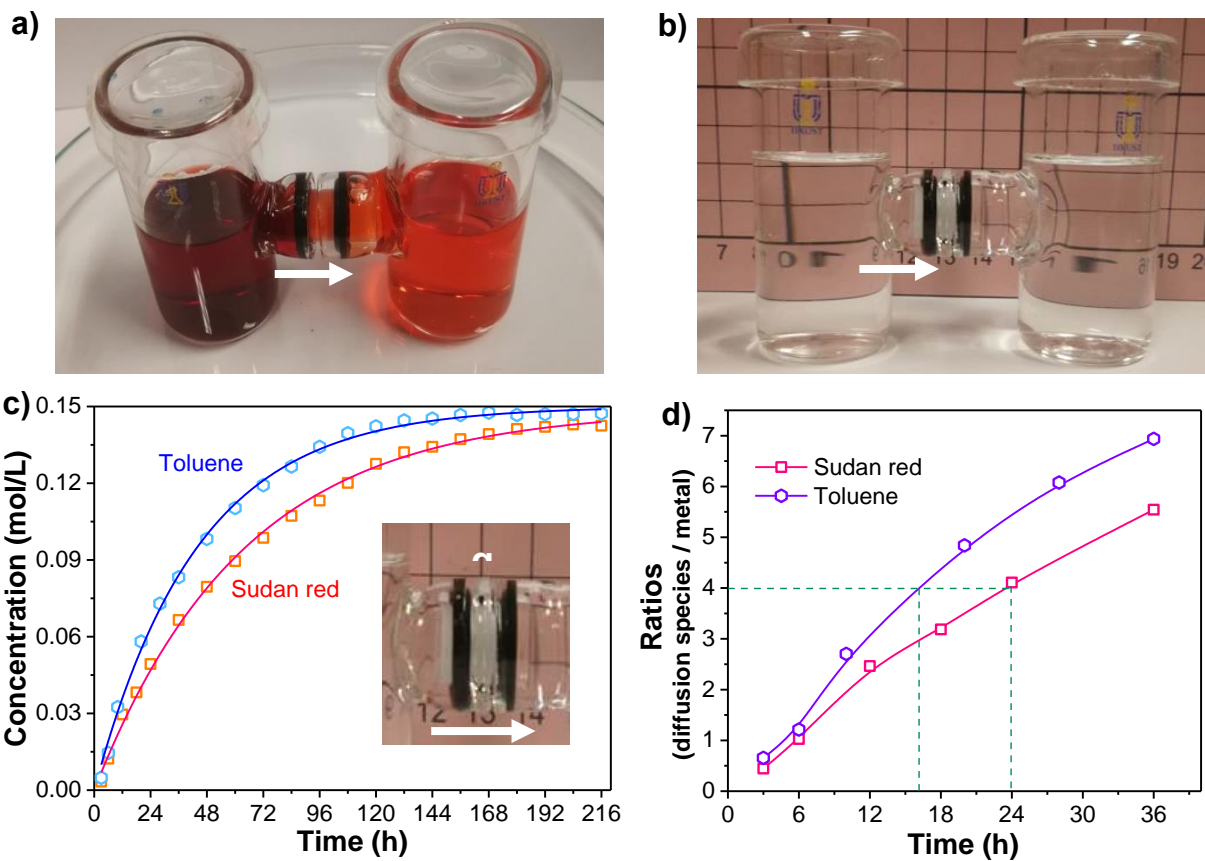


**Fig. S1.** Molecular diffusion through metal precursor gel. Photographs of the diffusion cell for diffusion study of Zn gel for (a) 0.3 M toluene in methanol, (b) 0.3 M Sudan red dye in methanol in left cell to pure methanol in right cell at 22 °C, (c) Plots of the concentration of toluene and Sudan red dye in right-hand cell with time, and (d) Molar ratios of sudan red and toluene to Zn passing through a Zn gel with time ( $\text{Mol}_{\text{Zn}}=1.2 \text{ mmol}$ , Zn gel diameter=6cm, length=8.8cm). Note: Analysis conducted by gas chromatography and UV-visible spectrophotometer.

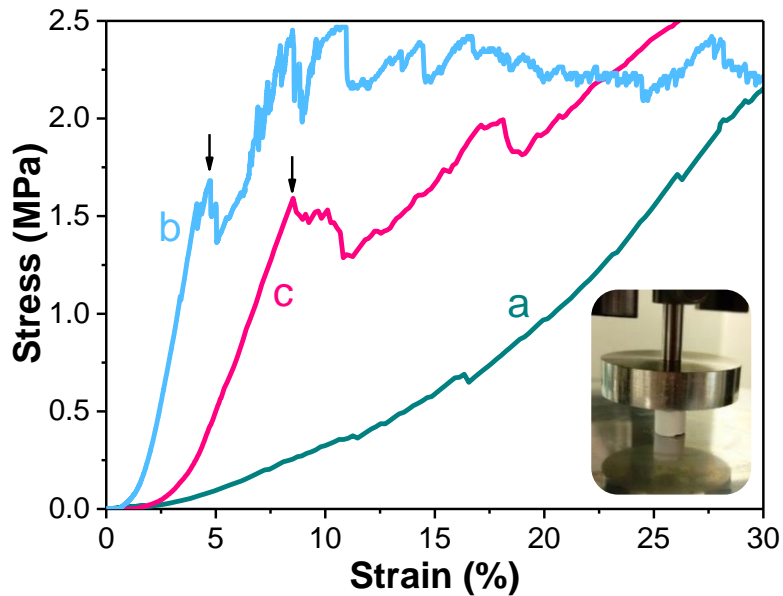


**Fig. S2.** Mechanical strengths of zinc precursor and MOF aerogels. The plots of stress-strain curves for (a) Zn precursor, (b) ZIF-8 (diameter=13.2mm, height=12mm), and (c) MOF-5 (diameter=12.8mm, height=11.4mm) aerogels displaying a linear compression followed by compaction that is the characteristic of porous solids. The arrows indicate the yield point for ZIF-8 (4.8 % strain) and MOF-5 (8.5 % strain) aerogels. The inset is a picture of the platform for axis compression test.

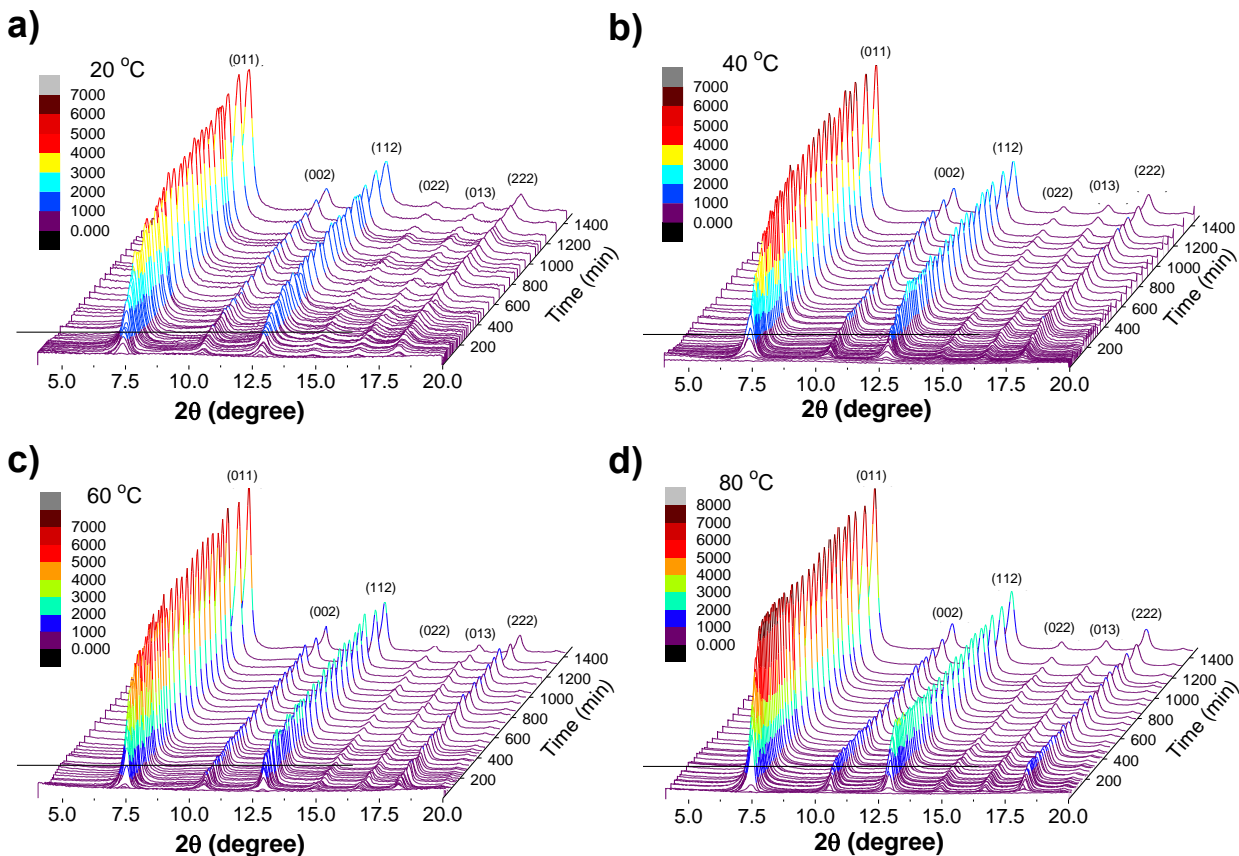


**Fig. S3.** Transformation of ZIF-8 from Zn precursor gel characterized by ex-situ XRD at 20°C (a), 40°C (b), 60°C (c), and 80°C (d) with the ZIF-8 characteristic diffraction peaks labelled. Elevated temperature promotes crystallisation and narrows down the peak widths, revealing enlarged crystal sizes. Note:  $m_{\text{gel}} = 0.089$  g Zn precursor gel with a thickness of ca. 50  $\mu\text{m}$ , Zn/Hmim mole ratio = 0.25, [Hmim] = 0.30 M, and  $V_{\text{soln}} = 5.0$  ml.

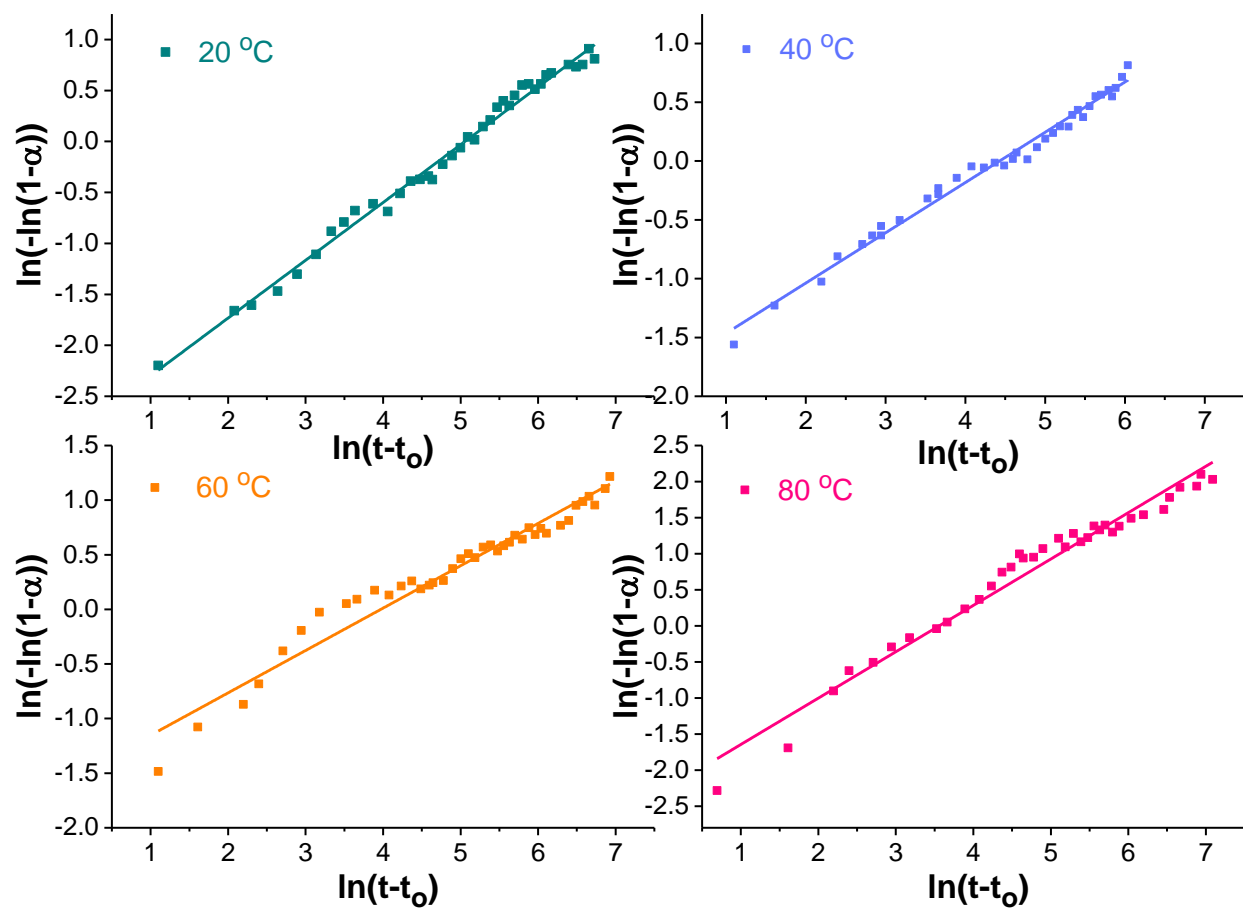


**Fig. S4.** Sharp-Hancock plots for the ZIF-8 crystallization from Zn precursor gel at different temperatures of 20°C, 40°C, 60°C, and 80°C.

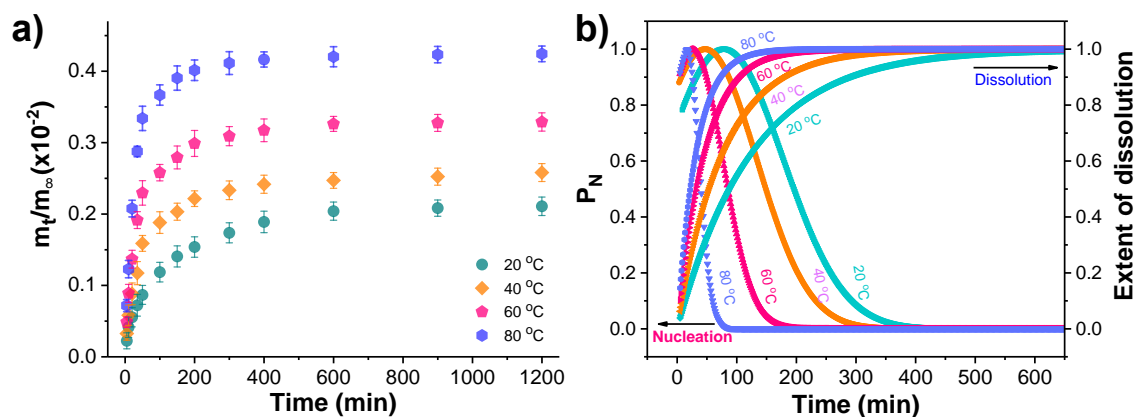


**Fig. S5.** Gel network dissolution during ZIF-8 transformation. (a) Plots of the dissolution of zinc from Zn precursor gels at 20°C, 40°C, 60°C, and 80°C, and the data fitting to a first order rate law (b-e), and the plots of nucleation probability and dissolution as a function of time (f), indicating coupled dissolution and nucleation during ZIF-8 crystallization from Zn precursor gel.

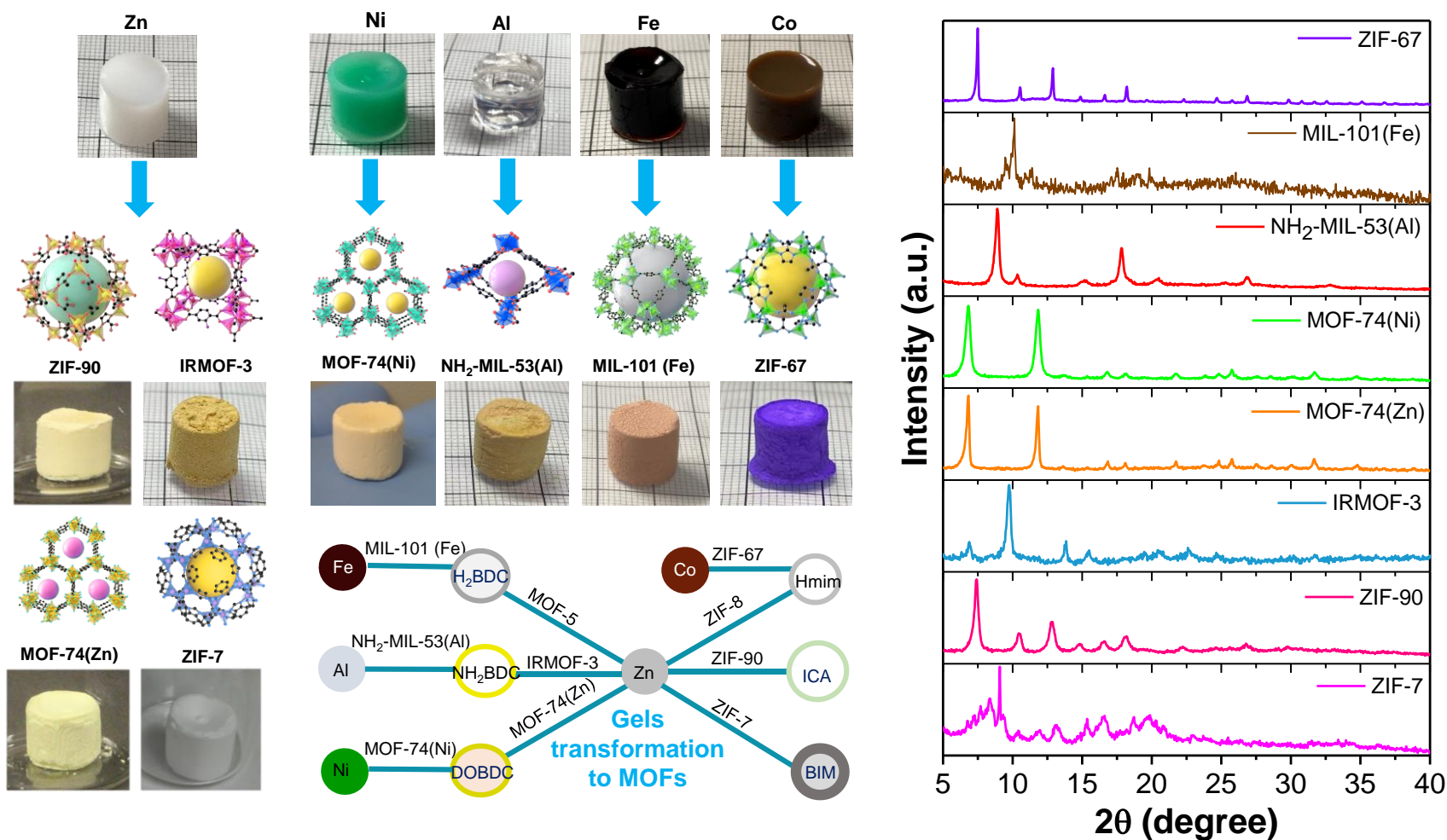


**Fig. S6.** Versatile preparation of MOF aerogels from metal precursor gels and their corresponding X-ray diffraction. The first-row photographs are Zn, Ni, Al, Fe, Co wet gels being transformed by reacting with suitable ligands into MOF aerogels. The sketch at the bottom right corner illustrates the conversion pathways from precursor gels to MOFs. Note: Zn: ZIF-90 (ICA: imidazole-2-carboxyaldehyde), ZIF-7 (BIM: benzimidazole), IRMOF-3 (NH<sub>2</sub>BDC: 2-aminoterephthalic acid), MOF-74 (DOBDC: 2,5-Dihydroxyterephthalic acid), NH<sub>2</sub>-MIL-53 (NH<sub>2</sub>BDC: 2-aminoterephthalic acid), MIL-101 (H<sub>2</sub>BDC: terephthalic acid), and ZIF-67 (Hmim: 2-methylimidazole).

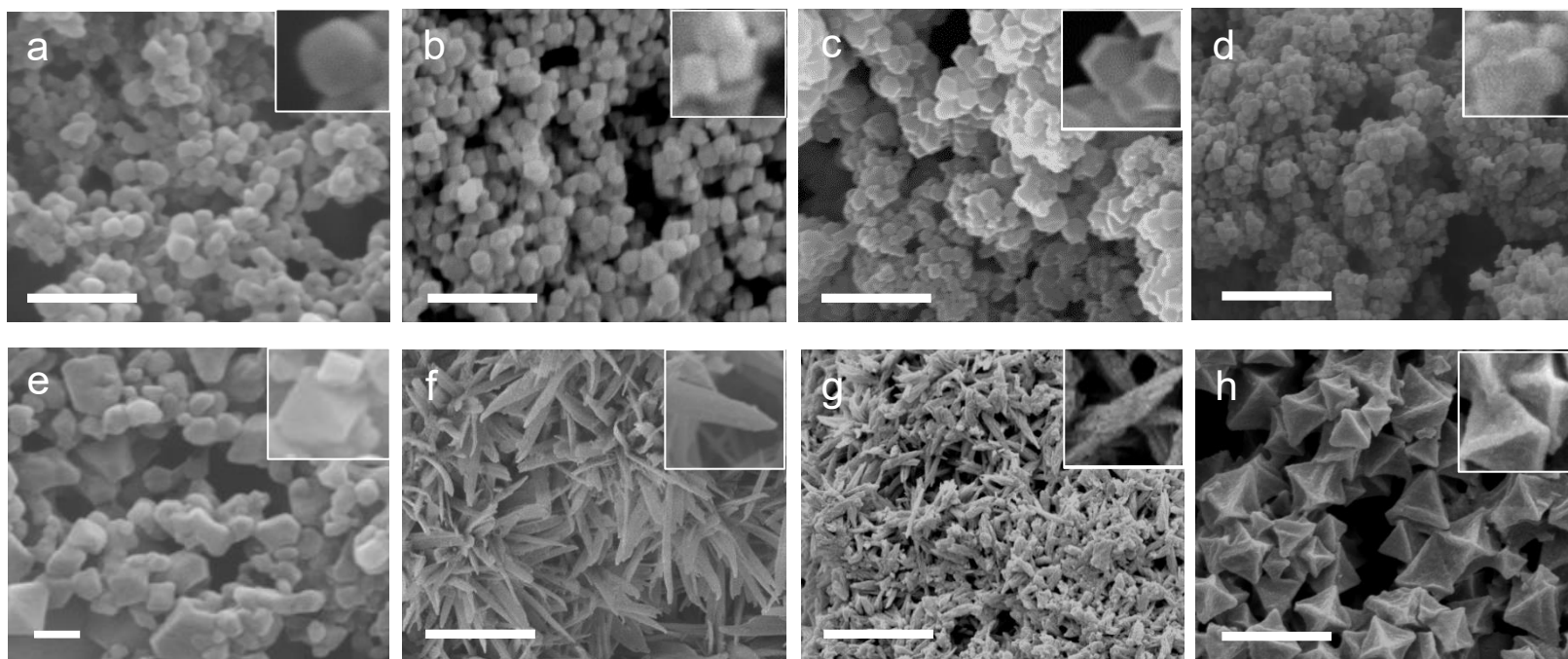


**Fig. S7.** SEM images of MOF aerogels prepared via pathway 2: (a) ZIF-8@60°C, (b) MOF-5@100°C, (c) ZIF-67@60°C, and (d) ZIF-90@60°C, and pathway 3: (e) HKUST-1, (f) MOF-74(Zn), (g) MOF-74(Ni), and (h) MIL-101(Fe). The scale bar is 500 nm except for (e) – 100 nm.

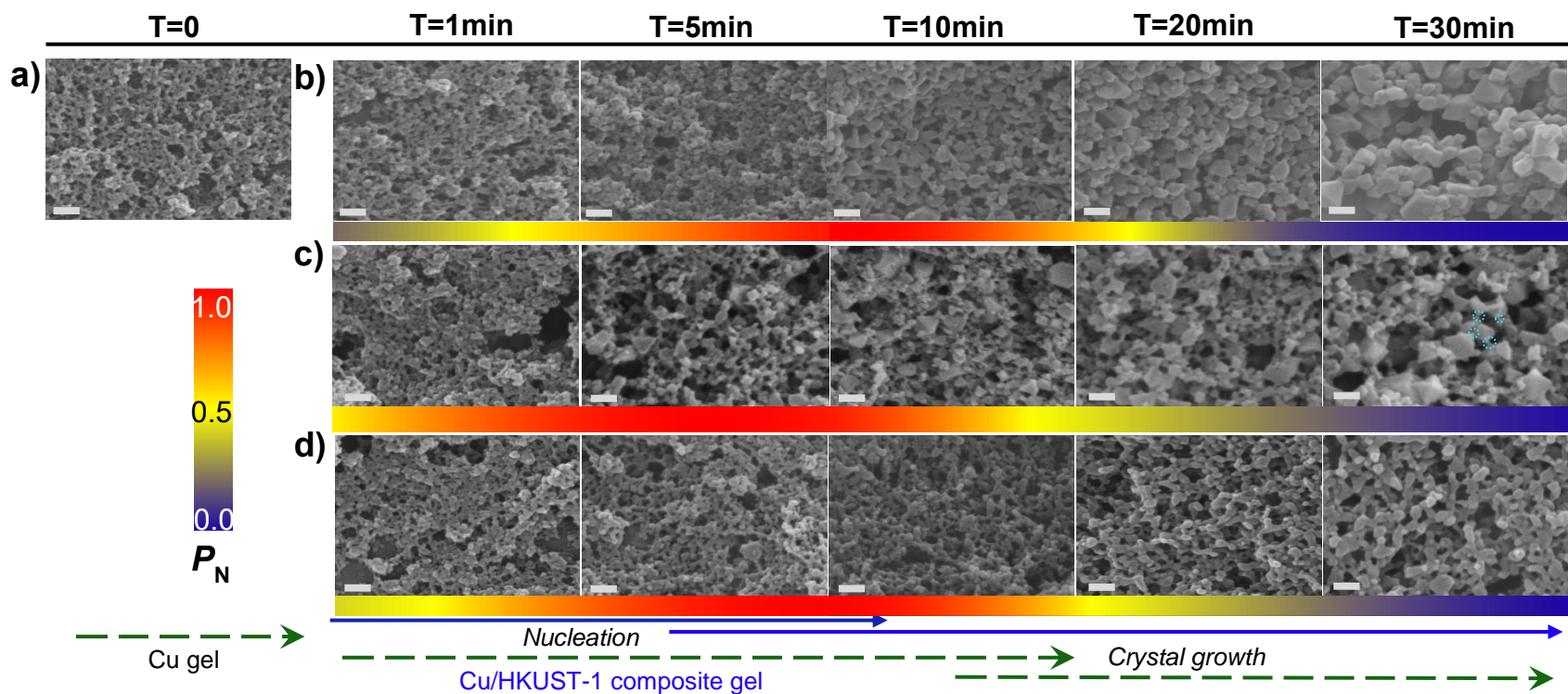


**Fig. S8.** Morphological transformation of Cu precursor gel to HKUST-1 at different conditions vs time. SEM images of Cu precursor gel (a) conversion into HKUST-1 after immersion the gel in (b) trimesic acid [TMA] = 0.05 M, (c) [TMA] = 0.35 M, (d) [TMA] = 0.05 M, [sodium formate] = 0.10 M. **The circles in the last image of Figure S8c indicate joint points of crystals.** The scale bar is 100 nm and the color bar denotes  $P_N$  (nucleation probability). The Cu precursor gels were in 30  $\mu\text{m}$  thickness, and the conversion was proceeded in ligand solution of 5 ml.

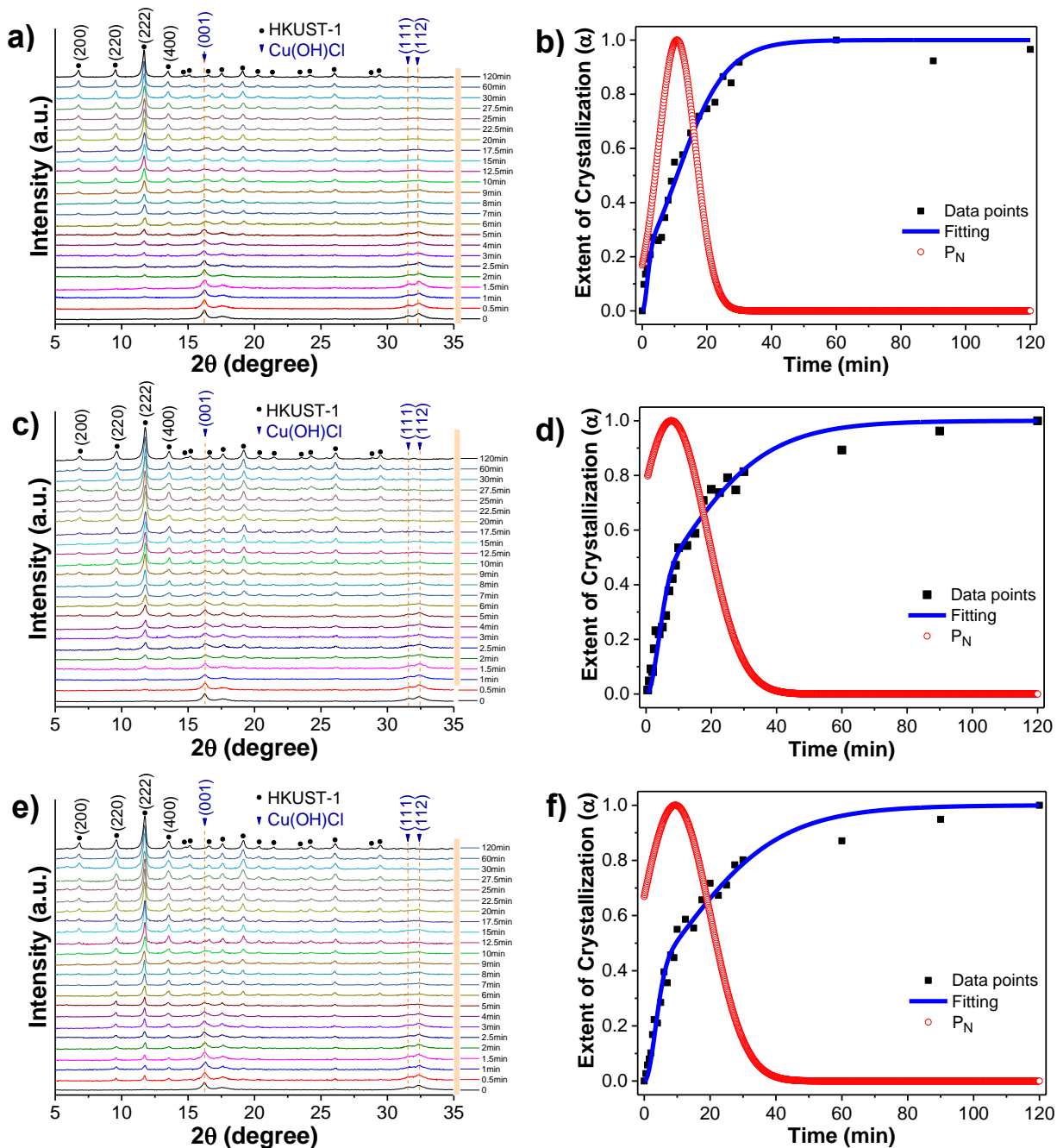


**Fig. S9.** HKUST-1 crystallization. X-ray diffraction of copper precursor gel conversion into HKUST-1 after immersion in (a)  $[TMA] = 0.05\text{ M}$ , (c)  $[TMA] = 0.35\text{ M}$ , (e)  $[TMA] = 0.05\text{ M}$ ,  $[\text{sodium formate}] = 0.10\text{ M}$ , and their corresponding plots (b, d, and f) of the non-linear least-square fits of the Gualtieri equation and the probability curves of nucleation ( $P_N$ ).

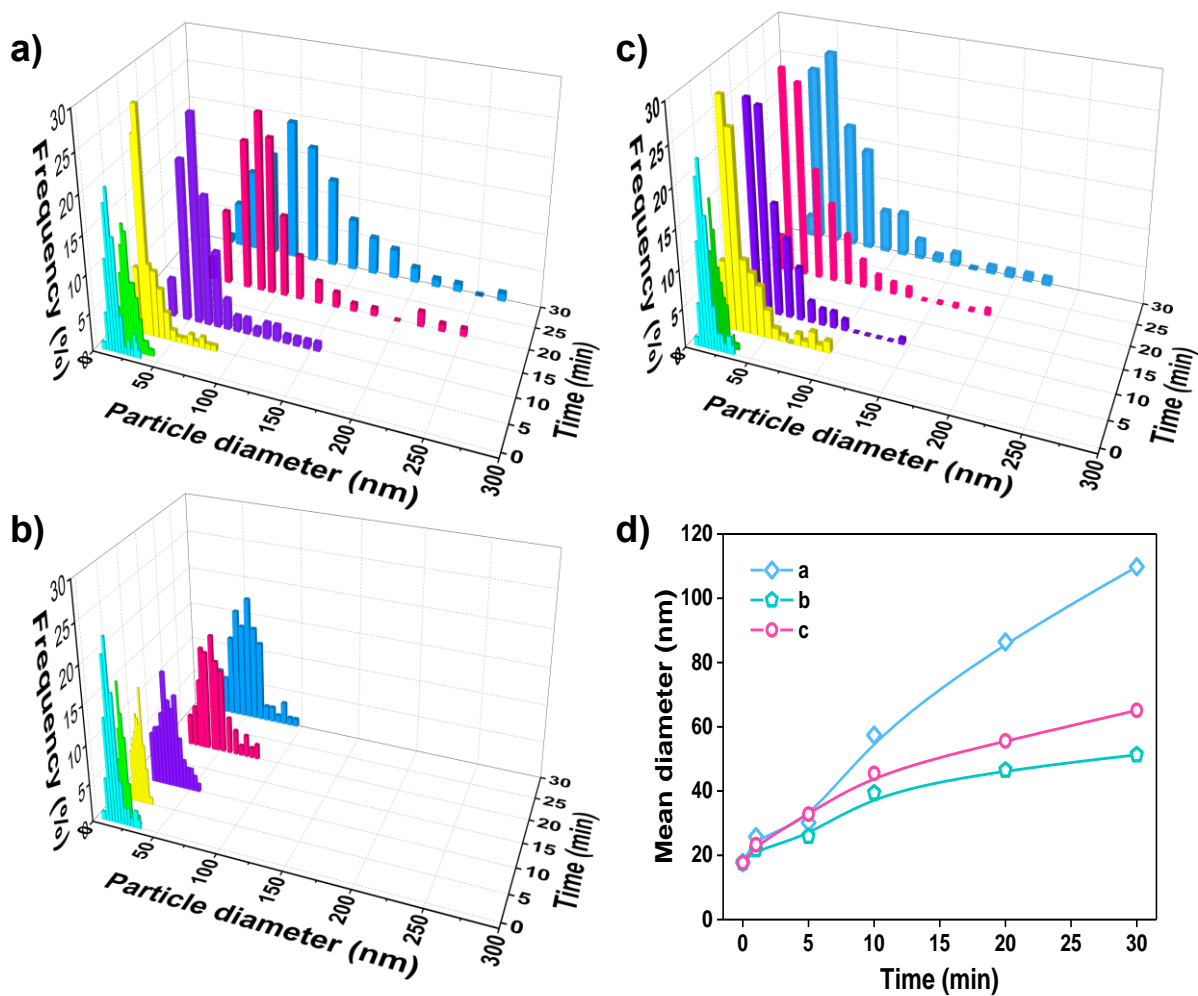


**Fig. S10.** HKUST-1 crystal growth in gel networks. Histograms of the particle size distributions during conversion of the copper precursor gel into HKUST-1 after immersion in (a) trimesic acid  $[TMA] = 0.05\text{ M}$ , (b)  $[TMA] = 0.35\text{ M}$ , (c)  $[TMA] = 0.05\text{ M}$ ,  $[sodium\ formate] = 0.10\text{ M}$ , and (d) mean diameters from particle size distributions of (a), (b), and (c) showing reduction of crystal sizes by changing reaction parameters. Note: Measurements were taken of 220-250 particles from SEM micrographs (Fig. S8) of the samples crystallized for various times.

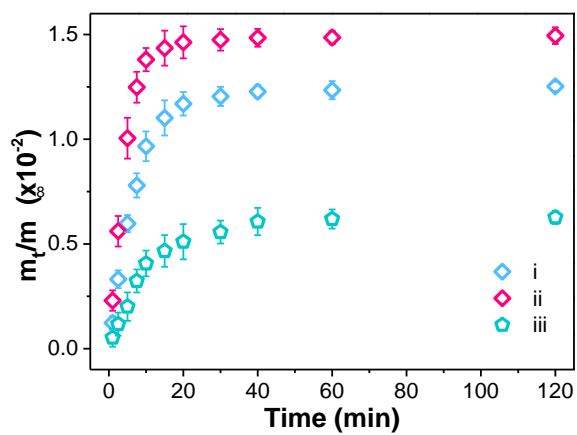


**Fig. S11.** Dissolution of copper precursor gel network during transformation into HKUST-1 in different conditions. (i) [TMA] = 0.05 M, (ii) [TMA] = 0.35 M, and (iii) [TMA] = 0.05 M, [sodium formate] = 0.10 M.

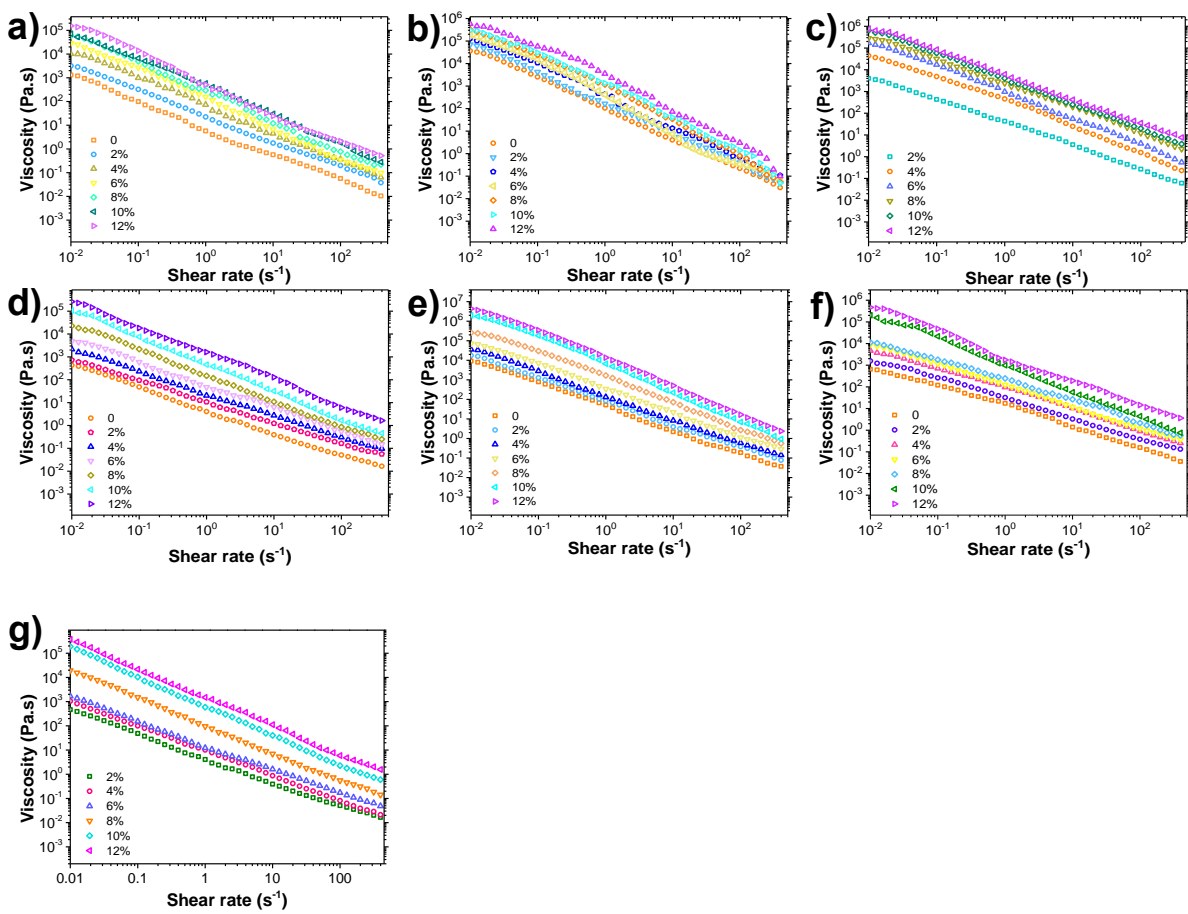


**Fig. S12.** Rheological properties of metal gels of Zn (a), Ni (b), Cu (c), Co (d), Fe (e), Al (f), and Eu(g) with addition of different amount of PAA (0-12wt.%).



**Fig. S13.** Sol-gel 3D-printer. A laboratory designed and built 3D printer with an advanced extrusion nozzle for precise printing of colloidal sol-gel materials.

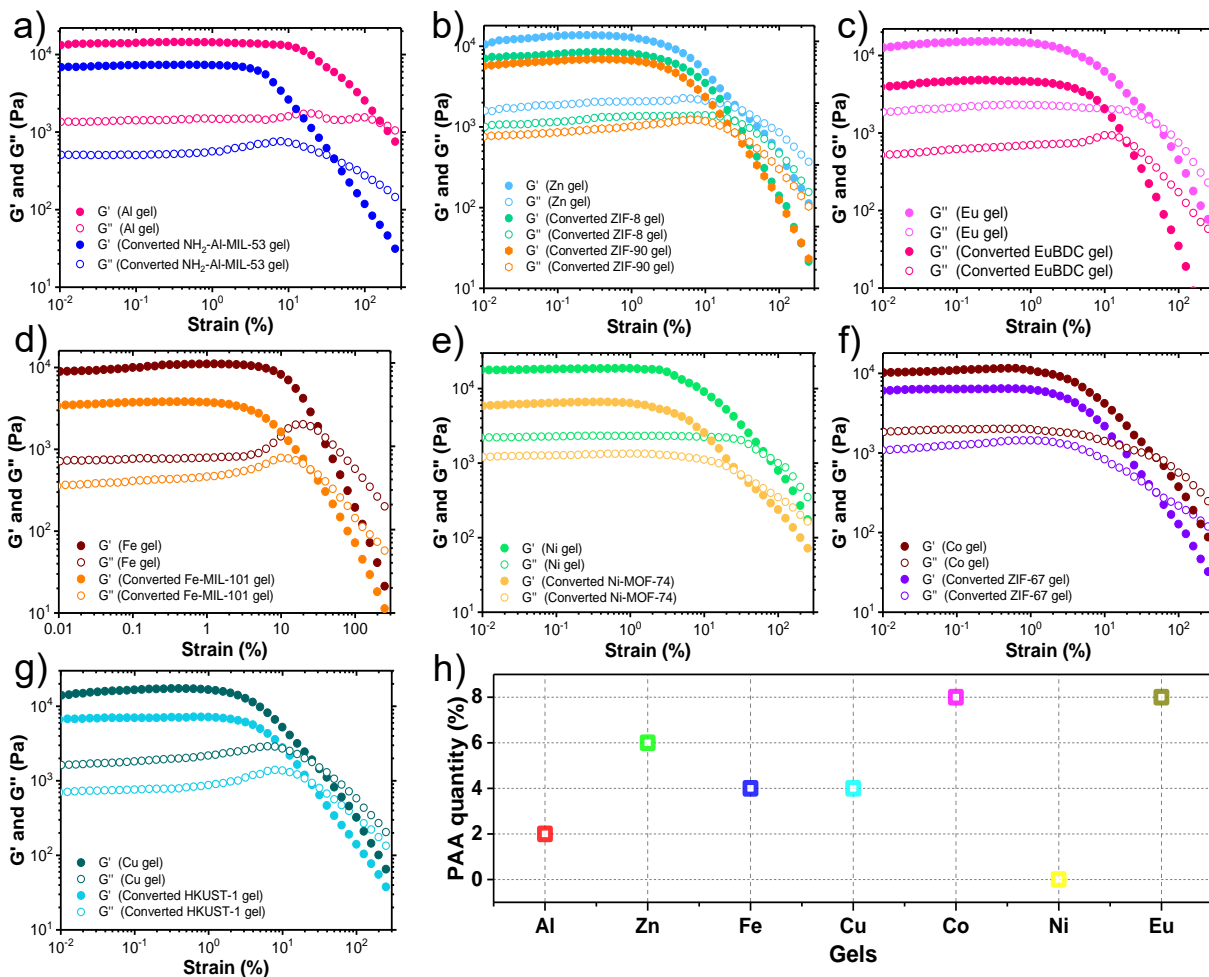


**Fig. S14.** Dynamic strain sweeps of metal gels and their converted MOF gels. Al gel and converted  $\text{NH}_2$ -MIL-53 (Al) gel (a), Zn gel and converted ZIF-8 and ZIF-90 gels (b), Eu gel and converted EuBDC gel (c), Fe gel and MIL-101 (Fe) gel (d), Ni gel and converted MOF-74(Fe) gel (e), Co gel and converted ZIF-67 gel (f), Cu gel and converted HKUST-1 gel (g), and PAA weight ratios in these metal gels (h). The Storage ( $G'$ ) and Loss ( $G''$ ) modulus are measured by oscillatory amplitude sweeps at strain of 0.01 to 500% and angular frequency of 1 rad/s). The critical yield strains are identified at the limit of the linear viscoelastic region of Storage Modulus ( $G'$ ).

## Supplementary Tables

**Table S1.** Preparation of Zn precursor gels.

Zn(NO <sub>3</sub> ) <sub>2</sub> ·6H <sub>2</sub> O (mmol)	ZnCl <sub>2</sub> (mmol)	PAA (wt.%)	Gelation time <sup>†</sup> (h)	Shrinkage (vol.%)	Appearance
0.70	0.10	0	14	8.6	turbid
0.65	0.15	0	12	2.2	turbid
0.60	0.20	0	9.0	3.5	turbid
0.65	0.15	0.1	4.3	1.8	turbid
0.65	0.15	0.4	1.5	0	turbid
0.65	0.15	0.8	0.8	0	turbid
0.65	0.15	1.6	0.6	0	turbid
0.65	0.15	3.2	0.3	0	turbid
0.65	0.15	6.4	0.5	0	turbid
0.65	0.15	8.0	1.3	0	translucent
0.80	-	8.0	1.6	0	turbid

<sup>†</sup> The gelation time is the time when the sol-gel mixture solidifies.

**Table S2.** FTIR band assignments for Zn precursor alcogel, ZIF-8 and MOF-5. <sup>7-10</sup>

Frequency (cm <sup>-1</sup> )	Band assignment	
400-580	$\nu$ Zn-O matrix	precursor
1408	$\nu_{\text{sym}}$ COO-	precursor
1454	$\nu$ CH <sub>2</sub>	precursor
1591 <sup>†</sup>	$\nu_{\text{asym}}$ COO-	precursor
1716	$\nu$ carbonyl (C=O)	precursor
421	$\nu$ Zn-N (ZnN <sub>4</sub> cluster of ZIF-8)	ZIF-8
660-800	$\delta_{\text{oop}}$ imidazole ring	ZIF-8
900-1300	$\delta_{\text{ip}}$ imidazole ring	ZIF-8
1350-1500	$\nu$ imidazole ring	ZIF-8
1585	$\nu$ C=N	ZIF-8
517	$\nu$ Zn-O (Zn <sub>4</sub> O cluster of MOF-5)	MOF-5
730-1120	$\nu_{\text{oop}}$ aromatic ring	MOF-5
1384	$\nu_{\text{sym}}$ carboxylate (COO-)	MOF-5
1480-1680	$\nu_{\text{asym}}$ carboxylate (COO-)	MOF-5
1718	$\nu$ carbonyl (C=O)	MOF-5

<sup>†</sup>The band is assigned to COO<sup>-</sup> complexed to Zn<sup>2+</sup>

Note:  $\nu$ -stretch vibration;  $\delta$ -bending; *ip*-in-plane; *oop*-out-of-plane; *sym*-symmetric; *asym*-asymmetric

**Table S3.** Textural properties of freestanding porous MOFs, silica, and carbon materials.

Materials	Terms <sup>†</sup>	$\rho$ (g/cm <sup>3</sup> )	$S_{\text{BET}}$ (m <sup>2</sup> /g)	$V_{\text{Micro}}$ (cm <sup>3</sup> /g)	$V_{\text{tot}}$ (cm <sup>3</sup> /g)	Pore Structure	Morph.	Ref.
ZIF-8	nanocrystals	-		0.532	-	micro	-	11
MOF-5	nanocrystals	-		-	-	-	-	12
ZIF-8	monolith	1.14	1359	0.532	-	macro	packing	13
MOF-5	monolith	0.79	~1500	-	~0.72	-	packing	14
MOF-74(Ni)	monolith	-	737	0.32	-	meso/macro	packing	15
UiO-66-NH <sub>2</sub>	monolith	-	370	0.16	-	meso/macro	continuous	16
HKUST-1	monolith	-	1240	0.561	-	macro	packing	17
HKUST-1	monolith	-	1315	-	-	macro	continuous	18
UiO-66	monolith	0.430	1177	0.46	1.62	meso	packing	18
UiO-66	xerogel	0.386	1459	0.47	2.09	meso/macro	packing	19
UiO-66	aerogel	-	1255	0.33	1.66	meso	packing	19
HKUST-1	monolith	1.06	1193	0.51	0.52	meso/macro	Packing	20
MIL-100(Fe)	aerogel	-	1618	0.72	-	macro	packing	20
Al-BDC	aerogel	0.638	1250	0.43	1.10	meso	continuous	21
Al-BTC	aerogel	0.576	1443	0.42	1.17	meso	continuous	21
Silica	aerogel	0.142	824	-	-	meso	continuous	22
Carbon	aerogel	0.00075	272	-	-	macro	continuous	23
ZIF-8	aerogel	0.157	1312	0.423 <sup>‡</sup>	1.35 <sup>#</sup>	meso/macro	continuous	this work
ZIF-8*	xerogel	0.434	1269	0.449 <sup>‡</sup>	0.684 <sup>#</sup>	mes-/macro	packing	this work
MOF-5	aerogel	0.184	1456	0.476 <sup>‡</sup>	1.47 <sup>#</sup>	mes-/macro	continuous	this work

<sup>†</sup>terminology according to references; <sup>‡</sup> measured at P/P<sub>0</sub> = 0.1; <sup>#</sup> measured at P/P<sub>0</sub> = 0.99. \*Sample prepared by 3D printing. Note: ( $S_{\text{BET}}$ )-BET surface area; ( $\rho$ )-density ( $\rho$ ), micropore volume ( $V_{\text{Micro}}$ ), Total pore volume ( $V_{\text{Total}}$ ), Pore features, and morphology structures of reported porous monolithic MOFs and our MOF aerogels.

**Table S4.** ZIF-8 crystallization rate kinetics according to Avrami–Erofe'ev equation.

T/°C	$t_0^{\dagger}$	$\alpha$ (120 min) <sup>#</sup>	$n^{\ddagger}$ (SH)	$C^{\S}$	$r^2$	k (SH)
20	2	0.550	0.567	-2.87	0.988	$6.28 \times 10^{-3}$
40	2	0.640	0.427	-1.89	0.984	$1.20 \times 10^{-2}$
60	1	0.720	0.401	-1.61	0.952	$1.80 \times 10^{-2}$
80	1	0.920	0.713	-2.48	0.970	$3.09 \times 10^{-2}$

<sup>†</sup>the induction time; <sup>#</sup>extent of crystallization @120min; <sup>‡</sup>Avrami exponent; <sup>§</sup>intercept of linear SH fitting.

**Table S5.** ZIF-8 crystallization rate kinetics according to Gualtieri equation.

T/°C	<i>a</i> /min	<i>b</i>	$k_n$ (min <sup>-1</sup> ) <sup>†</sup>	$k_g$ (min <sup>-1</sup> ) <sup>‡</sup>	$r^2$
20	78.3(5)	87.4(8)	0.012(8)	0.064(5)	0.965(4)
40	54.2(2)	56.1(2)	0.018(4)	0.136(6)	0.973(7)
60	26.4(3)	21.4(9)	0.037(8)	0.203(9)	0.962(4)
80	17.3(8)	15.2(5)	0.061(0)	0.278(4)	0.982(1)

<sup>†</sup>nucleation rate constant, <sup>‡</sup>crystallization rate constant.

**Table S6.** Zinc dissolution from precursor gels according to a first order rate law.

T/°C	$k_d$ (min <sup>-1</sup> )	$r^2$
20	$7.65 \times 10^{-3}$	0.943
40	$1.59 \times 10^{-2}$	0.937
60	$3.11 \times 10^{-2}$	0.933
80	$3.89 \times 10^{-2}$	0.929

**Table S7.** Preparation of aluminum, nickel, iron, cobalt, copper, and europium precursor gels.

Metal salts <sup>†</sup>	Solvent/Vol. (ml)	H <sub>2</sub> O (ml)	PO <sup>#</sup> (mmol)	PAA (wt.%)	time	Shrinkage (vol.%)
Al(NO <sub>3</sub> ) <sub>3</sub> ·9 H <sub>2</sub> O	Methanol/1.0	0.25	6	2	36-44 h	0
Co(NO <sub>3</sub> ) <sub>2</sub> ·6 H <sub>2</sub> O	Ethanol/0.65	0.10	4	6	28-34 h	0
CuCl <sub>2</sub> ·2 H <sub>2</sub> O	Ethanol/0.5	0	4	6	3 min	0
EuCl <sub>3</sub> ·6 H <sub>2</sub> O	Ethanol/1.1	0.3	6	8	2h	0
Fe(NO <sub>3</sub> ) <sub>3</sub> ·6 H <sub>2</sub> O	Ethanol/1.15	0.15	6	4	2 min	0
NiCl <sub>2</sub> ·6 H <sub>2</sub> O	Methanol/1.25	0.10	8	0	12-16 h	0
Zn salts	Ethanol/1.25	0	8	3.2	24 min	0

<sup>†</sup>Metal salt is 0.6mmol except Zn salts are 0.65 mmol Zn(NO<sub>3</sub>)<sub>2</sub>·6 H<sub>2</sub>O and 0.15 mmol ZnCl<sub>2</sub>; <sup>#</sup>propylene oxide.

**Table S8.** Preparation of MOF gels/aerogels from their respective metal precursor gels.

Gels	MOF	Ligand	Solvent	[Ligand] (M)	T(°C)/t(h)
Zn	ZIF-7	BIm	DMF	0.2	60/36
Zn	ZIF-90	ICA	DMF	0.3	80/36
Zn	IRMOF-3	NH <sub>2</sub> BDC	DMF	0.15	60/36
Zn	MOF-74	DOBDC	THF: H <sub>2</sub> O	0.2	60/36
Al	NH <sub>2</sub> -MIL-53	NH <sub>2</sub> BDC	5 DMF: H <sub>2</sub> O	0.1	95/48
Ni	MOF-74	DOBDC	3 DEF: 2 Ethanol: H <sub>2</sub> O	0.2	80/48
Fe	MIL-101	H <sub>2</sub> BDC	5 DMF: H <sub>2</sub> O	0.1	98/72
Co	ZIF-67	Hmim	Methanol	0.25	25/36
Cu	HKUST-1	TMA	1Ethanol:1H <sub>2</sub> O	0.35	

Note: BIm (Benzimidazole), ICA (2-Imidazolecarboxaldehyde), NH<sub>2</sub>BDC (2-Aminoterephthalic acid), DOBDC (2,5-dioxido-1,4-benzenedicarboxylate), H<sub>2</sub>BDC (Terephthalic acid), Hmim (2-methylimidazol), TMA (trimesic acid)

**Table S9.** HKUST-1 crystallization rate kinetics according to Gualtieri equation.

Variables	$a/min$	$b$	$k_n (\text{min}^{-1})^\dagger$	$k_g (\text{min}^{-1})^\ddagger$	$r^2$
i	10.7(6)	8.0(7)	0.093 (0)	0.413(4)	0.974(7)
ii	9.4(4)	14.9(0)	0.105(9)	0.236(3)	0.979(9)
iii	7.7(5)	15.2(7)	0.129(1)	0.185(9)	0.975(6)

<sup>†</sup>nucleation rate constant, <sup>‡</sup>crystallization rate constant.

Note: i) [TMA] = 0.05 M; ii) [TMA] = 0.05 M, [sodium formate] = 0.10 M; iii) [TMA] = 0.35 M

**Table S10.** Copper dissolution from precursor alcogels according to a first order rate law.

T/°C	$k_d$ (min <sup>-1</sup> )	$r^2$
i	$1.33 \times 10^{-1}$	0.978
ii	$8.97 \times 10^{-2}$	0.962
iii	$1.72 \times 10^{-1}$	0.983

Note: i) [TMA] = 0.05 M; ii) [TMA] = 0.05 M, [sodium formate] = 0.10 M; iii) [TMA] = 0.35 M

## References

1. F. Millange, R. El Osta, M. E. Medina and R. I. Walton, *CrystEngComm*, 2011, **13**, 103-108.
2. M. Avrami, *J. Chem. Phys.*, 1939, **7**, 1103-1112.
3. M. J. Van Vleet, T. Weng, X. Li and J. Schmidt, *Chem. Rev.*, 2018, **118**, 3681-3721.
4. A. Gualtieri, *Phys. Chem. Miner.*, 2001, **28**, 719-728.
5. E. L. Cussler, *Diffusion: mass transfer in fluid systems*, Cambridge university press, 2009.
6. A. Hahn, G. Brandes, P. Wagener and S. Barcikowski, *J. Control. Release*, 2011, **154**, 164-170.
7. B. Civalieri, F. Napoli, Y. Noel, C. Roetti and R. Dovesi, *CrystEngComm*, 2006, **8**, 364-371.
8. L. J. Kirwan, P. D. Fawell and W. van Bronswijk, *Langmuir*, 2003, **19**, 5802-5807.
9. P. Li, Z. P. Xu, M. A. Hampton, D. T. Vu, L. Huang, V. Rudolph and A. V. Nguyen, *J. Chem. Phys. C*, 2012, **116**, 10325-10332.
10. Y. Hu, H. Kazemian, S. Rohani, Y. Huang and Y. Song, *Chem. Commun.*, 2011, **47**, 12694-12696.
11. Y. Pan, Y. Liu, G. Zeng, L. Zhao and Z. Lai, *Chem. Commun.*, 2011, **47**, 2071-2073.
12. L. Huang, H. Wang, J. Chen, Z. Wang, J. Sun, D. Zhao and Y. Yan, *Microporous Mesoporous Mater.*, 2003, **58**, 105-114.
13. T. Tian, J. Velazquez-Garcia, T. D. Bennett and D. Fairen-Jimenez, *J. Mater. Chem. A*, 2015, **3**, 2999-3005.
14. J. Purewal, D. Liu, J. Yang, A. Sudik, D. Siegel, S. Maurer and U. Müller, *Int. J. Hydrog. Energy*, 2012, **37**, 2723-2727.
15. H. Thakkar, S. Eastman, Q. Al-Naddaf, A. A. Rownaghi and F. Rezaei, *ACS Appl. Mater. Interfaces*, 2017, **9**, 35908-35916.
16. S. M. Vilela, P. Salcedo-Abraira, L. Micheron, E. L. Solla, P. G. Yot and P. Horcajada, *Chem. Commun.*, 2018, **54**, 13088-13091.
17. A. Ahmed, M. Forster, R. Clowes, P. Myers and H. Zhang, *Chem. Commun.*, 2014, **50**, 14314-14316.
18. N. Moitra, S. Fukumoto, J. Reboul, K. Sumida, Y. Zhu, K. Nakanishi, S. Furukawa, S. Kitagawa and K. Kanamori, *Chem. Commun.*, 2015, **51**, 3511-3514.
19. B. Bueken, N. Van Velthoven, T. Willhammar, T. Stassin, I. Stassen, D. A. Keen, G. V. Baron, J. F. Denayer, R. Ameloot and S. Bals, *Chem. Sci.*, 2017, **8**, 3939-3948.
20. T. Tian, Z. Zeng, D. Vulpe, M. E. Casco, G. Divitini, P. A. Midgley, J. Silvestre-Albero, J.-C. Tan, P. Z. Moghadam and D. Fairen-Jimenez, *Nat. Mater.*, 2018, **17**, 174-179.
21. L. Li, S. Xiang, S. Cao, J. Zhang, G. Ouyang, L. Chen and C.-Y. Su, *Nat. Commun.*, 2013, **4**, 1774.
22. C. A. Morris, M. L. Anderson, R. M. Stroud, C. I. Merzbacher and D. R. Rolison, *Science*, 1999, **284**, 622-624.
23. H. Sun, Z. Xu and C. Gao, *Adv. Mater.*, 2013, **25**, 2554-2560.